



# The Effects of Solidification Cooling and Growth Rates on Microstructure and Hardness of Supersaturated Al-7%Si-x%Zn Alloys

Rafael Kakitani, Camila Konno, Amauri Garcia, and Noé Cheung

Submitted: 3 August 2021 / Revised: 12 September 2021 / Accepted: 6 October 2021 / Published online: 25 October 2021

There is a lack of information in the literature about the effects of the solidification cooling ( $\dot{T}$ ) and growth ( $v$ ) rates on both microstructure and mechanical properties of Al-Si-Zn alloys. Moreover, the relation between microstructural parameters and mechanical behavior is valuable information to evaluate the potential of Al-Si-Zn alloys. New applications can be attained when Zn is added to Al-Si alloys, due to the reduction in the *liquidus* temperature,  $T_L$ , and improvement in mechanical properties. The present study investigates the evolution of microstructure and the corresponding effects on microhardness of Al-7wt.%Si-(10, 15, 20) wt.%Zn alloys, directionally solidified under unsteady-state conditions. The microstructure of the Al-7%Si-x%Zn alloys is shown to be characterized by a dendritic  $\alpha$ -Al matrix, with the interdendritic region composed of  $\alpha$ -Al, Si, and an AlFeSi-type intermetallic. The decrease in  $\dot{T}$  and  $v$  resulted in coarsening of the dendrites. Dendritic scaling laws are experimentally determined relating primary, secondary, and tertiary dendritic spacings to  $\dot{T}$  and  $v$ . The main mechanism of reinforcement is shown to be related to the supersaturated solid solution. The hardness of the Al-7%Si-10%Zn alloy is not influenced by refinement of the dendritic spacings, however, each further increment of about 5% Zn to this alloy resulted in a hardness increase of about 30 HV.

**Keywords** Al-Si-Zn alloys, microstructure, microhardness, solidification

## 1. Introduction

The Al-Si alloys are one of the most versatile among the usual aluminum alloys being widely used in the automotive and aerospace sectors. In automobiles, the use of Al-Si alloys includes powertrain components, engine blocks, cylinder heads, pistons, and others (Ref 1, 2). In airplanes, these alloys are restricted to structural parts, such as rear frame, tail rotor gearbox, pipe heat exchanger, winglet, and canopy bracket (Ref 1, 3, 4). Other interesting applications can be found in thermal energy storage as a phase change material (Ref 5, 6), coating on steel for corrosion protection (Ref 7, 8), and as a potential candidate in hydrogen generation in fuel cells (Ref 9, 10).

New applications can be attained when Zn is added to Al-Si alloys, due to the reduction in the *liquidus* temperature,  $T_L$ , and improvement in mechanical properties. A low  $T_L$  is desirable in brazing, below the melting temperature of the base metals (substrate), to limit melting to only the filler metal. Moreover, the mechanical response of the filler should be, at least, close to that of the base metals, ensuring the reliability of the joint. In aluminum brazing, the filler metals usually melt below 610 °C and the commercial Al-12%Si alloy is the most commercially sold (Ref 11, 12). In the view of fillers being developed with

good compliance between high mechanical properties and an appropriate  $T_L$ , the Al-Si-Zn alloys have been a prominent choice. Initially, Suzuki and collaborators (Ref 13) studied the Al-4.2%Si-40%Zn eutectic alloy (along with this study, the solute content is by weight), finding a eutectic temperature of 535 °C and a microstructure composed by  $\alpha$ -Al, Si, and  $\eta$ -Zn phases. With a fixed Zn content at 40% and Si between 2 and 6%, Yang and collaborators (Ref 14), reached a maximum shear strength of 142.3 MPa, brazing 6061 plates with an Al-4%Si-40%Zn alloy. The highest microhardness was found in the alloy with 6%Si (~170 HV) and the value in the Al-4%Si-40%Zn alloy was around 150 HV. Although the good results, the high Zn content can lead to a brittle joint and the vapor pressure of Zn is high enough to damage the brazing equipment (Ref 13, 15). To avoid these issues and maintain the properties, quaternary alloys have been proposed, with decreasing Zn content and addition of either Cu or Ge (Ref 12, 16, 17). However, Ge is expensive and both alloying elements induce the precipitation of a high fraction of hard intermetallics, and, consequently, the joint becomes brittle.

The reinforcement provided by Zn is mainly through the solid solution in the soft  $\alpha$ -Al matrix and, according to the phase diagram, its maximum solubility is 83% at 381 °C, decreasing to less than 0.1% at room temperature (Ref 18). Although the solubility is low at room temperature and equilibrium conditions, higher levels of Zn in the  $\alpha$ -Al matrix have been reported in Al-Zn and Al-Si-Zn alloys (Ref 19–22), resulting in a supersaturated solid solution. The supersaturation was obtained by both slow solidification techniques, such as sand casting, and rapid solidification, such as melt spinning. Besides, as the Zn content in the alloy increased, the supersaturation also increased. Due to the enhancement of the

Rafael Kakitani, Camila Konno, Amauri Garcia, and Noé Cheung, University of Campinas, Campinas, São Paulo, Brazil. Contact e-mail: cheung@fem.unicamp.br.

mechanical strength of the  $\alpha$ -Al matrix, Al-Si-Zn alloys are gaining attention in tribological applications and components that require high tensile strength (Ref 23–26). Alemdağ and Beder (Ref 25) observed that the addition of only 4% Zn to the Al-7%Si alloy increased both hardness and tensile strength by more than 10%, and the volume loss in wear tests was reduced by 30%. The Al-6%Si-40%Zn alloy, solidified in gravity casting (Ref 23), showed a tensile strength of around 220 MPa, despite an elongation to fracture inferior to 1%. These Al-Si-Zn alloys exhibited superior mechanical behavior when compared with some commercial cast Al alloys, such as AA242, AA295, AA355, and AA712 (Ref 27).

In this sense, the Al-Si-Zn alloys fulfill the requirements of filler metals and high-strength alloys, as well as they can be chosen in terms of appropriate Si and Zn contents, which allows the development of an alloy for both applications. The high Si content in the commercial Al-12%Si filler alloy favors the formability, due to the high fraction of the  $\alpha$ -Al + Si eutectic (Ref 28), but the corrosion resistance is impaired. The addition of Zn increases the corrosion resistance in Al-Si alloys (Ref 29) and, according to Robles-Hernandez and collaborators (Ref 1), 15% of Zn is the limit to achieve good mechanical properties. However, for brazing purposes, an amount higher than 15% is interesting with a view to reducing  $T_L$ .

To the best of the present authors' knowledge, there is a lack of information in the literature about the influence of the solidification thermal parameters on the microstructure and mechanical properties of Al-Si-Zn alloys. Moreover, the relation between microstructural parameters and mechanical behavior is valuable information to evaluate the potential of Al-

Si-Zn alloys. Therefore, this study aims to investigate the evolution of microstructure and the corresponding effects on microhardness of Al-7%Si-(10, 15, 20)%Zn alloys, directionally solidified under unsteady-state conditions. Through the unsteady-state solidification, the alloys are subjected to a wide range of growth rates,  $v$ , and cooling rates,  $\dot{T}$ , covering conditions found in the cooling step of the brazing process (0.2–1.7 °C/s (Ref 30)) and different types of casting. In previous studies with Al-based alloys subjected to directional solidification (Ref 31–33), it was reported that such process promoted the following ranges of thermal parameters:  $v = 0.1$ –1.5 mm/s and  $\dot{T} = 0.2$ –40 °C/s. Along such ranges of  $v$  and  $\dot{T}$ , it is possible to envisage a significant evolution of the length scale of the phases forming the microstructure, thus permitting correlations between microstructure features and microhardness to be developed.

## 2. Experimental Procedure

The partial pseudo-binary phase diagram of the Al-Si-Zn system, calculated by the Thermo-Calc software (TTAL5 database), is shown in Fig. 1(a) with the indication of the Al-7%Si- $x$ %Zn alloys (where  $x = 10, 15,$  and  $20$ ). The liquidus temperatures of all alloys are below 600 °C, and in thermodynamic equilibrium, the final microstructure of the alloys, according to the phase diagram, is composed of the  $\alpha$ -Al matrix, Si, and  $\eta$ -Zn phases. Table 1 shows the composition of the elements, of commercial purity, used to prepare the alloys.

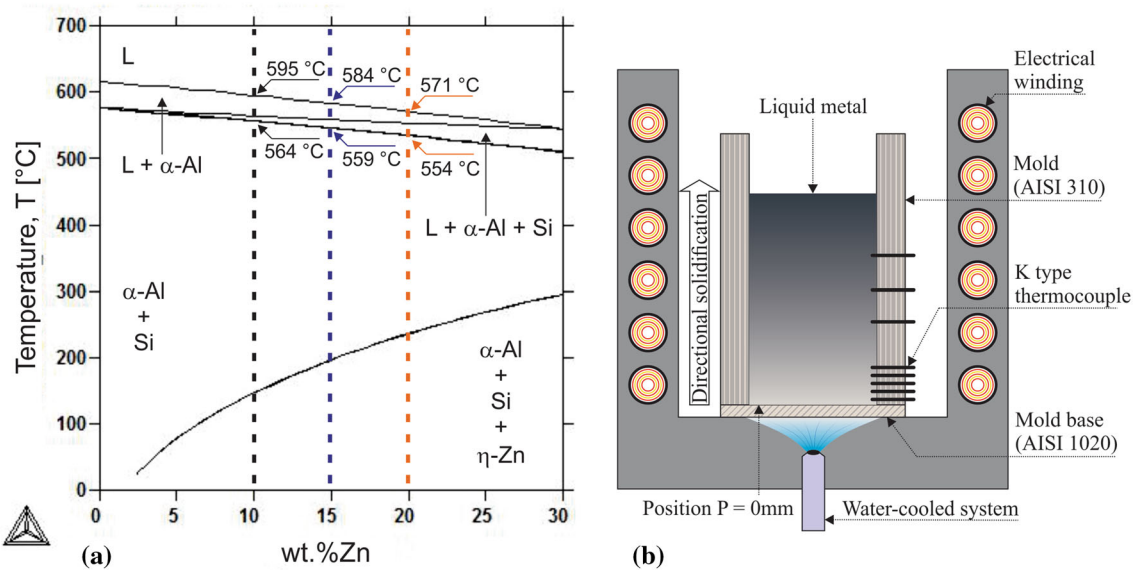


**Fig. 1** (a) Al-7%Si- $x$ %Zn partial phase diagram calculated by the Thermo-Calc software (TTAL5 database) and (b) directional solidification system

**Table 1** Composition of the metals used to prepare the Al-Si-Zn alloys

wt. %	Al	Si	Zn	Fe	P	Ca	Cu	Pb	Cd
Al	Balance	0.05	0.001	0.07	...	...	...	...	...
Si	0.25	Balance	...	0.49	0.009	0.31	...	...	...
Zn	0.0001	...	Balance	0.0007	...	...	0.0008	0.001	0.0008

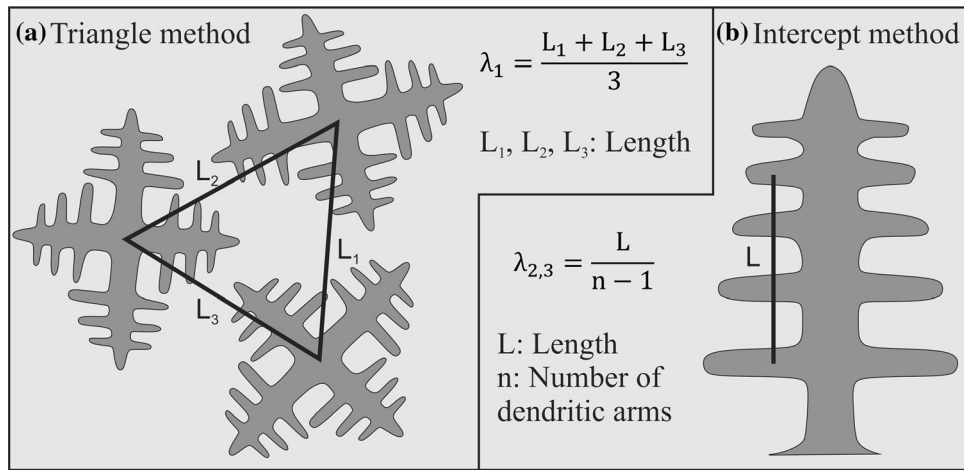


Fig. 2 Measurement of dendritic spacings through the (a) triangle method and (b) intercept method

Table 2 Comparison between the *solidus* and *liquidus* temperatures from the Thermo-Calc software (TTAL5 Database) and the experimental slow solidification

Alloy	Thermo-Calc		Experimental	
	$T_L$ , °C	$T_S$ , °C	$T_L$ , °C	$T_S$ , °C
Al-7%Si-10%Zn	595	564	591	559
Al-7%Si-15%Zn	584	559	581	555
Al-7%Si-20%Zn	571	554	578	558.5

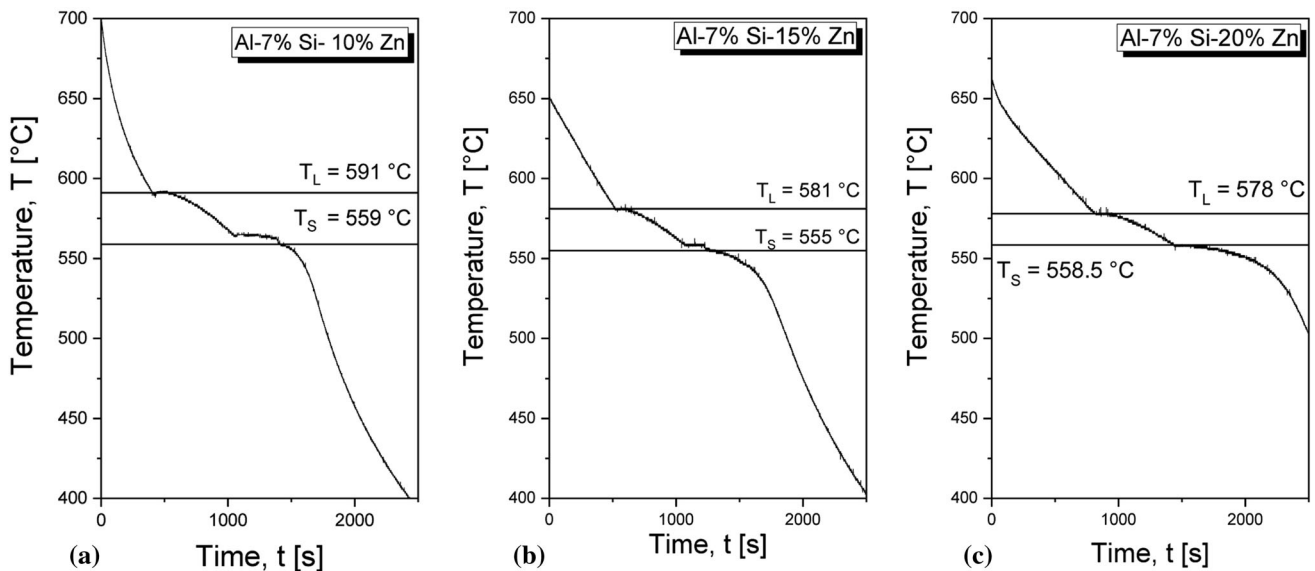
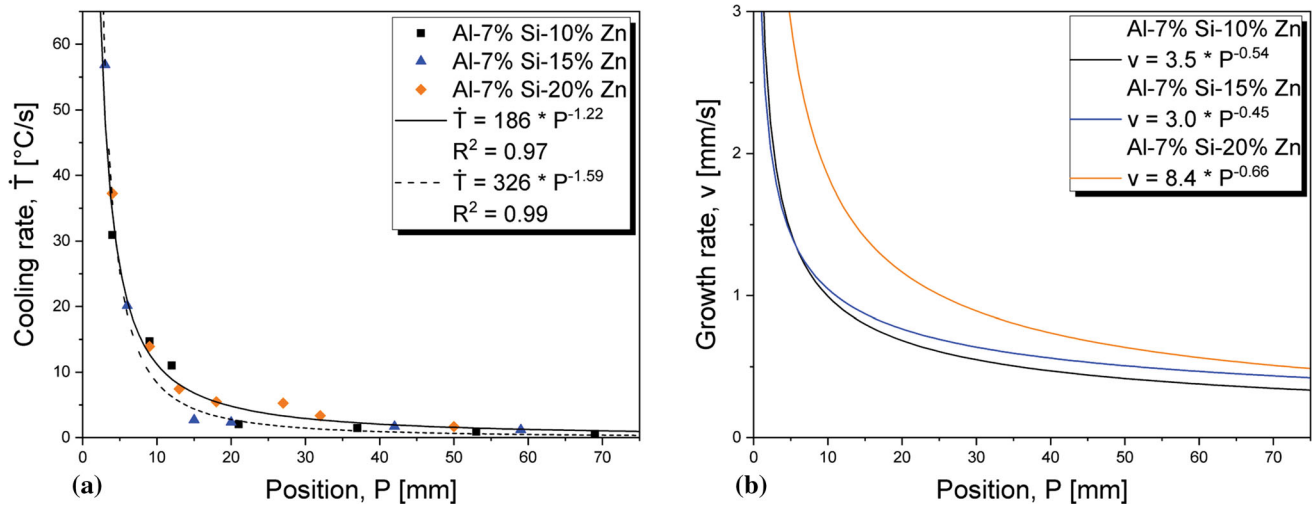


Fig. 3 Cooling profiles during slow solidification ( $\sim 0.1$  °C/s) of: (a) Al-7%Si-10%Zn, (b) Al-7%Si-15%Zn and (c) Al-7%Si-20%Zn alloys

At first, pieces of Al were melted at 800 °C in a muffle furnace. Fragments of Si were then added to molten Al and the mixture was put again into the furnace at 800 °C for 1 h to ensure the complete Si dissolution. Manual agitation, by using a coated alumina stainless steel rod bar, was used to favor homogenization in intervals of 20 minutes when the crucible was taken from the furnace and then returned into the furnace. After this time, pieces of Zn were added to the molten alloy and the same mentioned procedure used for Si incorporation was applied.

Before pouring the alloy into the mold of the directional solidification system, Argon was injected for 2 min in the liquid metal, forcing the flotation of impurities and removing trapped gases. A little portion of the liquid alloy was poured into a crucible pre-heated at 700 °C. The crucible was covered with insulated material and air-cooled. A K-type thermocouple, inserted inside the crucible, was used to record the temperature evolution of the alloy during the resulting slow solidification.



**Fig. 4** Profiles of: (a) cooling rate and (b) growth rate against position from the cooled surface of the Al-7%Si-x%Zn alloys ingots.  $R^2$  is the coefficient of determination

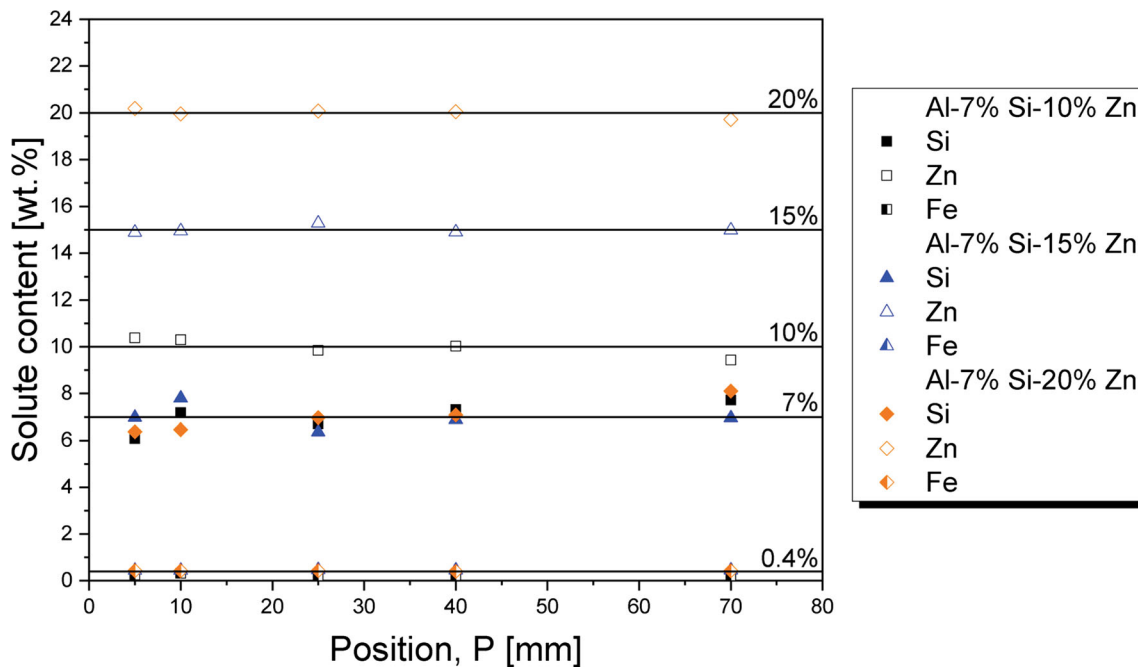


**Fig. 5** Solute distribution along the length of the Al-7%Si-x%Zn alloys ingots

The phase transformations were noticed when there was either an undercooling or change in slope of the cooling curve.

A split cylindrical mold (Fig. 1b) made of AISI 310 stainless steel, with an internal diameter of 60 mm, height of 160 mm, and wall thickness of 7 mm was used. The bottom part of the mold is closed with a 3 mm thick low carbon steel sheet. For the insertion of thermocouples, the mold contains 8 lateral holes of  $\varnothing 1.8$  mm, arranged at different positions,  $P$ , along the length of the mold, taking as reference the cooled base of the mold. The inner walls of the cylindrical mold were covered with alumina, in order to prevent direct contact of the molten metal with the mold walls, as well as to reduce lateral heat losses. The mold with the set of K-type thermocouples was placed inside a furnace. Electrical windings promoted a melt superheating of

about 10% above the *liquidus* temperature, which was switched off before the water-cooled system was turned on impinging the bottom part of the mold, leading to a vertical upward directional solidification. Thermal history during solidification was recorded at a frequency of 5 Hz in a computer attached to a Lynx ADS1000 data logger, which was connected to the thermocouples. The thermal history was used to determine the solidification cooling and growth rates, according to the time at which the *liquidus* isotherm passed by each thermocouple position along the length of the casting.  $\dot{T}$  and  $v$  were, respectively, calculated by the first derivatives with respect to time of both temperature vs. time ( $T \times t$ ) and position vs. time ( $P \times t$ ).



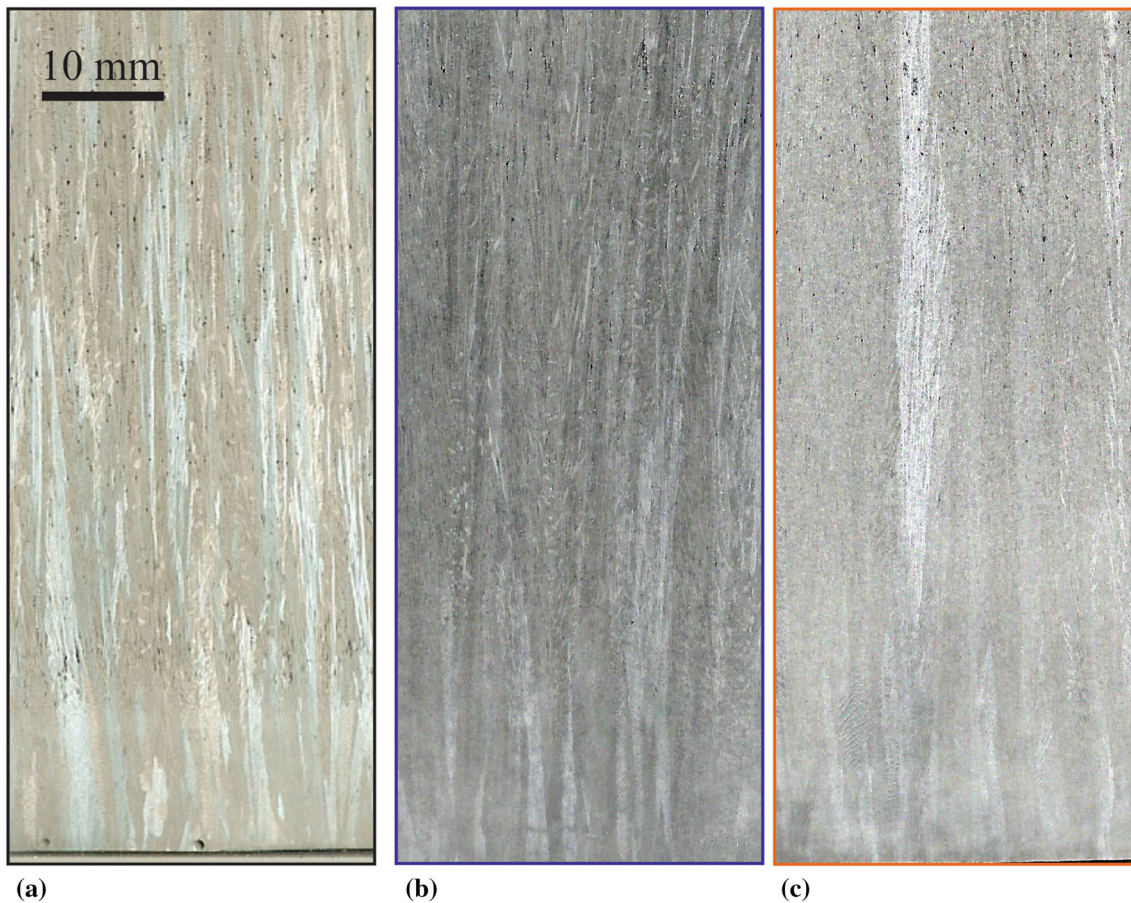


**Fig. 6** Macrostructures of directionally solidified alloys ingots: (a) Al-7%Si-10%Zn, (b) Al-7%Si-15%Zn and (c) Al-7%Si-20%Zn

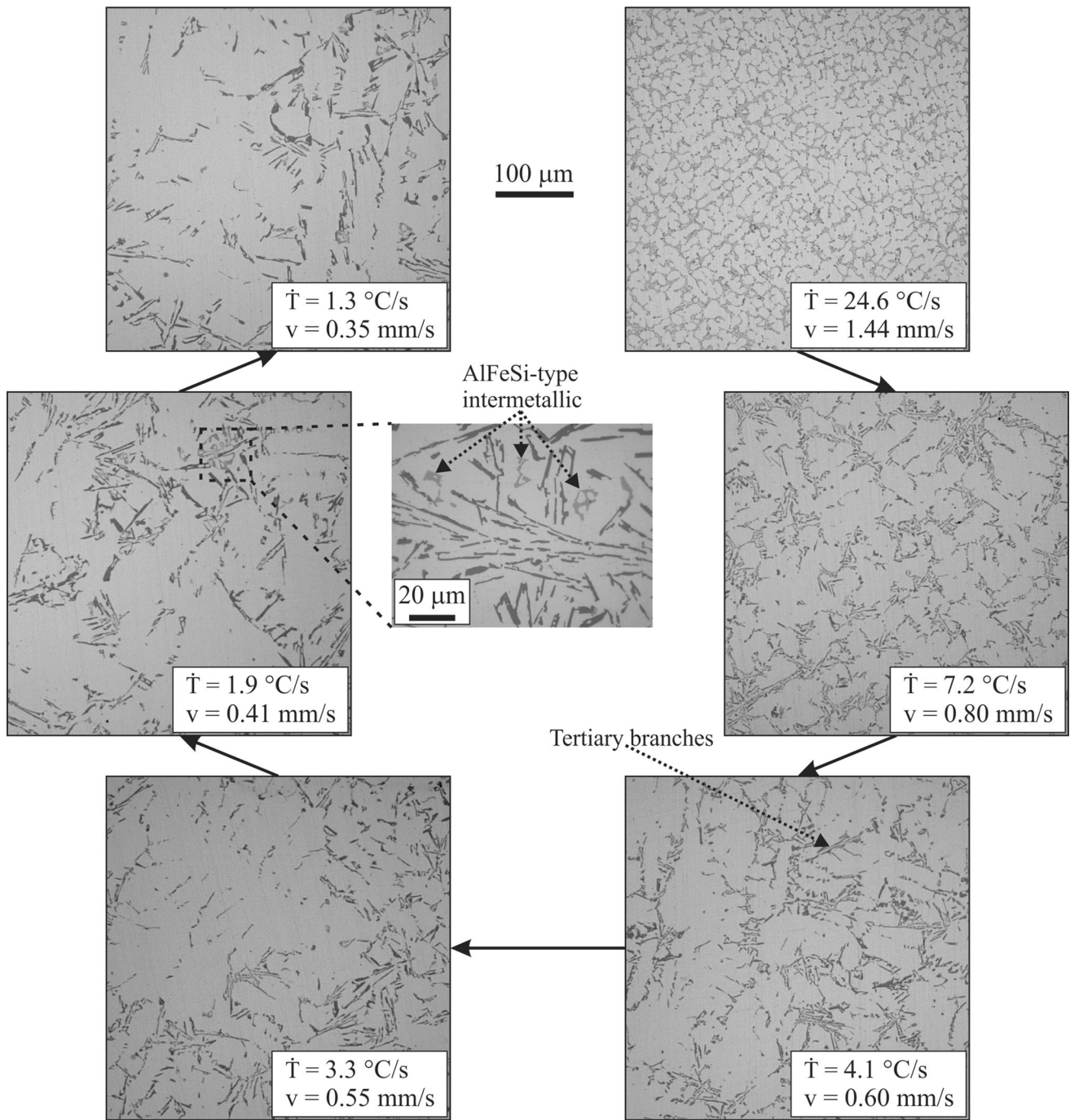
After solidification, the cylindrical directionally solidified (DS) ingot was longitudinally sectioned. One of the half-cylindrical parts was ground with 100 to 400 grit SiC papers and subsequently etched with an aqua regia solution, composed of HCl and HNO<sub>3</sub>, in the ratio of 3:1, in order to reveal the macrostructure. Selected transverse and longitudinal sections were ground with 100-1200 grit SiC papers, polished with 3 to 1/4 μm diamond pastes, and etched with 0.5% HF in aqueous solution in order to visualize the microstructure via an Olympus GX41 optical microscope. Images of the microstructures parallel and perpendicular to the vertical growth direction were used to measure the primary,  $\lambda_1$ , secondary,  $\lambda_2$ , and tertiary,  $\lambda_3$ , dendritic arm spacings.  $\lambda_1$  was measured using the triangle method while  $\lambda_2$  and  $\lambda_3$  were measured using the intercept method (Ref 34), being at least 30 measurements performed for each spacing type per sample. The measurement methods are shown in Fig. 2. The microstructure was also analyzed via a ZEISS EVO-MA15 scanning electron microscope coupled to an Oxford X-Max energy-dispersive X-ray spectrometer. X-ray diffraction (XRD) spectra were obtained using a Panalytical, X'pert Pro MRD XL model diffractometer with a 2-theta range from 20° to 90°, Cu-K $\alpha$  radiation, and a wavelength of 0.15406 nm. Chemical analyses along the length of the DS ingots were performed by an x-ray fluorescence spectrometer XRF-1800 model from Shimadzu. An FV-800 model from Future-Tech hardness tester was used with a load of 500 gf and a dwell time of 15 s, according to specifications of ASTM Standard E384, in order to determine the hardness of the samples extracted along

the length of the castings. At least 20 measurements on each sample were performed.

### 3. Results and Discussion

As can be seen in the cooling temperature profiles during slow solidification (cooling rate of ~0.1 °C/s) of the Al-7%Si-x %Zn alloys (Fig. 3), the increase in the alloy Zn content was able to reduce  $T_L$ , but the *solidus* temperatures,  $T_S$ , did not exhibit significant changes. The efficiency of Zn in changing  $T_L$  was higher for the Al-7%Si-15%Zn alloy, with a variation of about 10 °C in relation to the Al-7%Si-10%Zn alloy. It is worth noting that the lowest solidification interval was achieved for the alloy with 20%Zn, while the increase of 15-20% in Zn content only reduced  $T_L$  by about 3 °C. A short solidification interval is useful for both castability and brazeability because it means lower hot tear susceptibility and improved flowability (Ref 35). In contrast, with the information from the phase diagram (Table 2), the experimental values of  $T_L$  and  $T_S$  presented differences of less than 1.3%. Since the common base metals employed in brazing are generally AA6061 and AA6063 alloys, with  $T_S$  of 592 °C and 615 °C, respectively (Ref 15), the Al-7%Si-10%Zn may not be an appropriate candidate as a filler alloy.

The experimentally determined profiles of the solidification thermal parameters for the DS alloys castings are depicted in



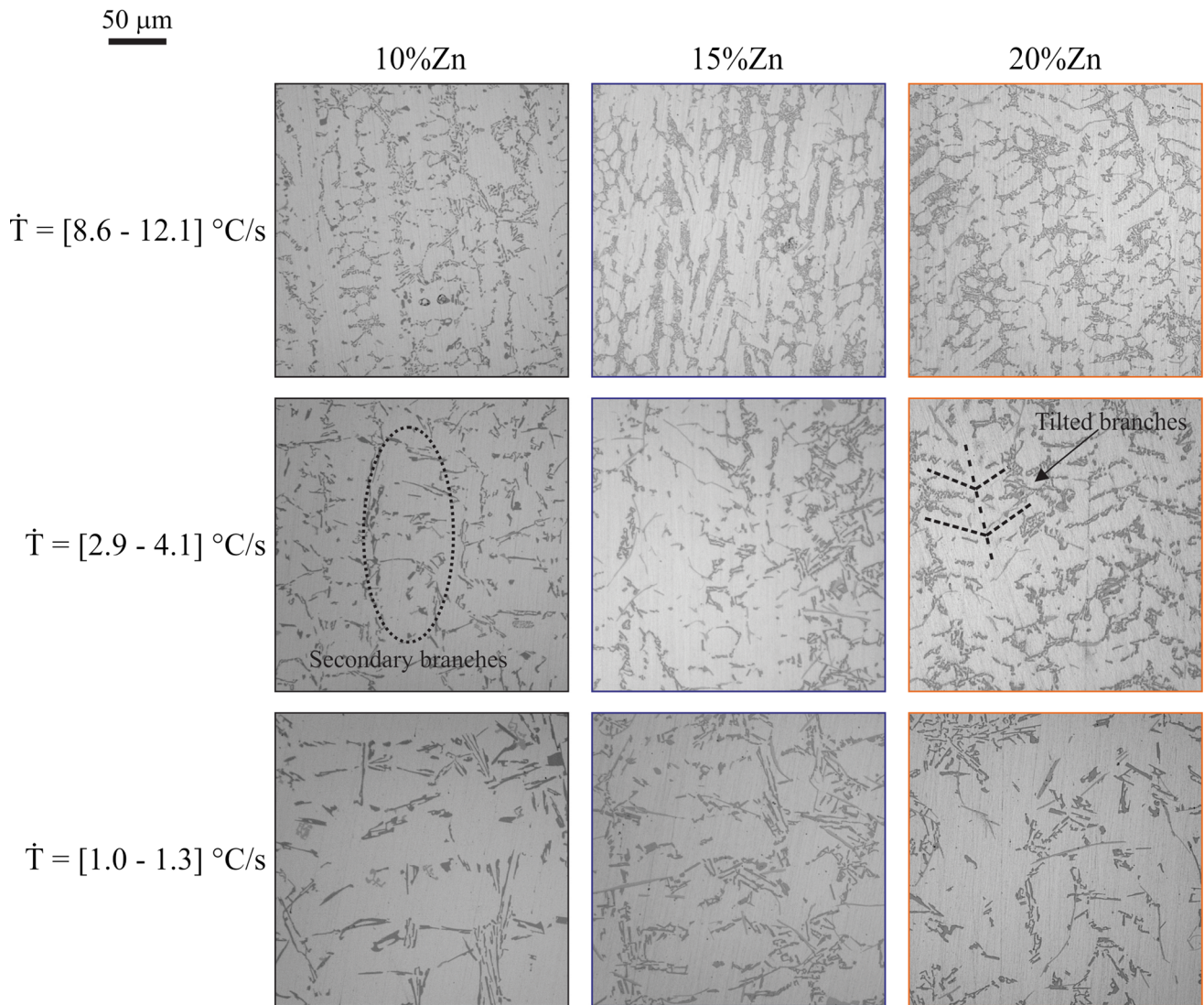
**Fig. 7** Evolution of microstructure in transverse samples of the Al-7%Si-10%Zn alloy ingot. The interdendritic region is shown in amplified detail.

Fig. 4, that is, the cooling rate,  $\dot{T}$ , and growth rate,  $v$ , versus position,  $P$ , along the length of the ingot. The reduction in  $\dot{T}$  and  $v$  from the cooled bottom to the top of the DS ingots was due to the increase in the thermal resistance of the system: in the early beginning of solidification, most of the metal is liquid and the thermal resistance is mainly associated with the thickness of the mold base; as the solidification progresses, both the evolution of the solid metal and the progressive development of an air gap between metal and mold, caused by thermal and volumetric contraction of the metal, decrease the heat flow extraction. Close to the water-cooled base of the mold ( $P = 0 \text{ mm}$ ), the

cooling rate profiles of the Al-7%Si- $x$ %Zn alloys ingots were similar, and for  $P > 10 \text{ mm}$ , a distinction can be noted among them. The Al-7%Si-10%Zn and Al-7%Si-20%Zn alloys ingots showed the same  $\dot{T}$  profile (solid line in Fig. 4a) and exhibited higher values than those of the Al-7%Si-15%Zn alloy (dashed line in Fig. 4a). This pattern was not observed in the  $v$  profiles (Fig. 4b), where different profiles were settled for each alloy ingot and the increase in the alloy Zn content seems to increase  $v$ . The experimentally determined values of  $\dot{T}$  and  $v$  refer to positions along the length of the ingots from 5 to 70 mm from the cooled bottom, so, the ranges of  $\dot{T}$  and  $v$  were  $[28.3\text{-}0.4] \text{ }^\circ\text{C/s}$



# Al-7%Si-Zn



**Fig. 8** Microstructure from longitudinal samples of the Al-7%Si-x%Zn alloys ingots

and [1.11-0.35] mm/s, respectively. Although the  $v$  profiles may be quite distinct among the length of the different alloy ingots, the  $\dot{T}$  profiles were almost the same, which seems curious since solidification occurs freely without any control. However, it is known that the cooling rate is the product of the thermal gradient ( $G$ ) and the growth rate, that is  $\dot{T} = G \cdot v$ . Thus, one can conclude that the thermal gradient profiles, obtained from this relationship, are also quite different among them.

The solute distribution along the length of the Al-7%Si-x%Zn alloy ingots can be seen in Fig. 5. For the three examined alloys ingots, Si is shown to present slight variation around 7%, whereas the Zn content remained close to the nominal composition. In general, the content of Fe detected by the XRF analysis was, on average, 0.4%, below the usual amount in commercial fillers. Certainly, the source of Fe was from residual content in Al and Si used to make the alloys and from the contact between the liquid metal and the bottom surface of the mold. In Al-Si alloys, the presence of Fe leads to the

precipitation of hard intermetallics, e.g.  $\beta$ -Al<sub>8</sub>FeSi,  $\alpha$ -Al<sub>12</sub>Fe<sub>3</sub>Si<sub>2</sub>, and  $\delta$ -Al<sub>4</sub>FeSi<sub>2</sub> (Ref 36, 37), that can increase both ultimate tensile strength and hardness of the material but, certainly the plastic behavior is reduced. In particular, the  $\beta$ -AlFeSi has the most deleterious effect because of the plate-like morphology and large size, increasing the tendency of crack propagation.

In Fig. 6, the macrostructure of the DS Al-7%Si-x%Zn alloys ingots can be observed. The grains of the three alloys ingots were predominantly columnar, without a trace of equiaxed grains. In hypoeutectic Al-Si and Al-Zn alloys, the literature reports a columnar-to-equiaxed transition (CET) when  $\dot{T} < 0.3 \text{ } ^\circ\text{C/s}$  (Ref 38, 39). At first, until  $P = 70 \text{ mm}$ , the alloys presented a  $\dot{T}$  higher than  $0.3 \text{ } ^\circ\text{C/s}$ , but even in the remaining part of the ingots, the transition was not noticed.

The microstructure of the Al-7%Si-x%Zn alloys was characterized by a dendritic  $\alpha$ -Al matrix, with the interdendritic region composed of  $\alpha$ -Al, Si, and an AlFeSi-type intermetallic. The decrease in  $\dot{T}$  and  $v$  resulted in the coarsening of the

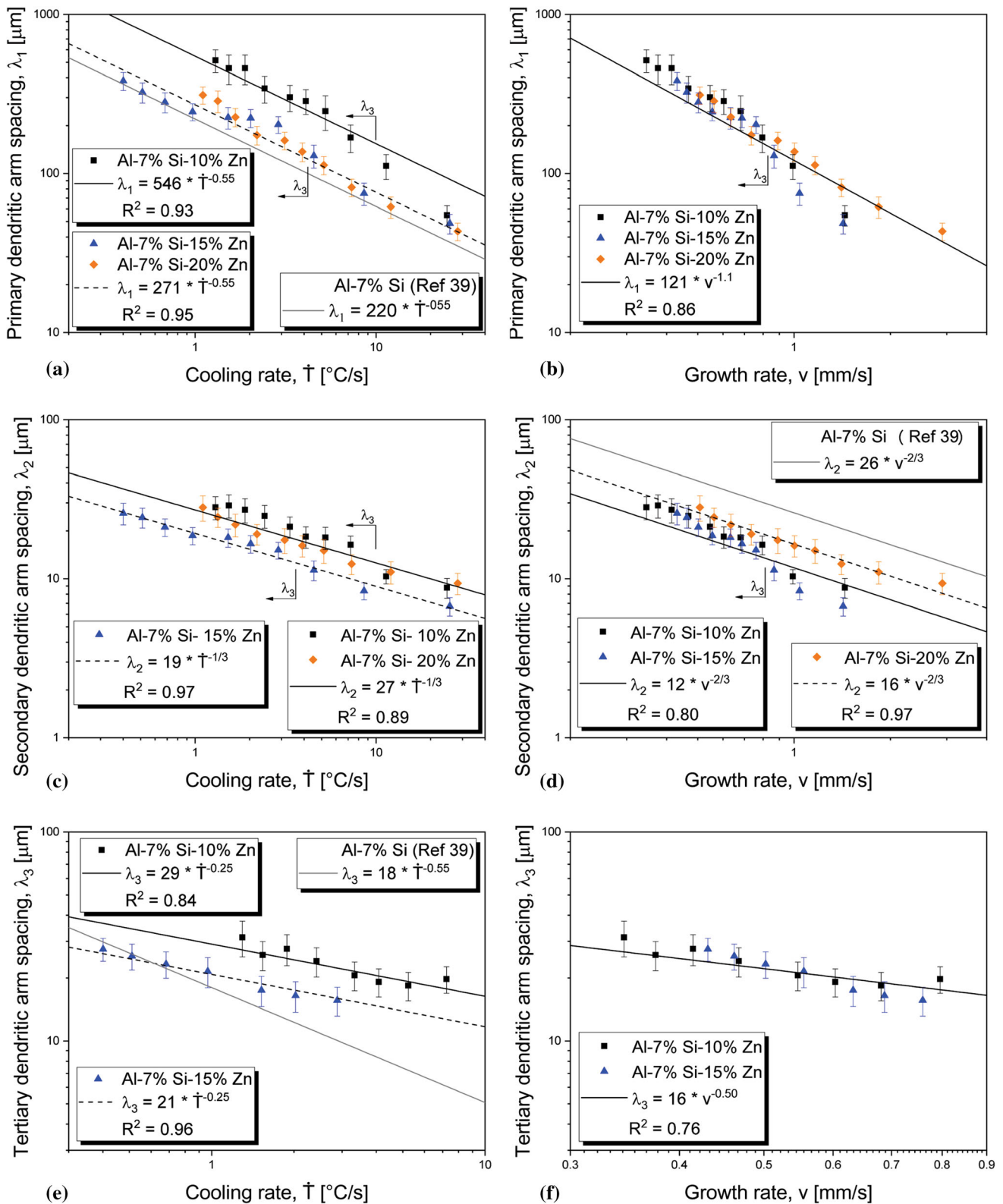
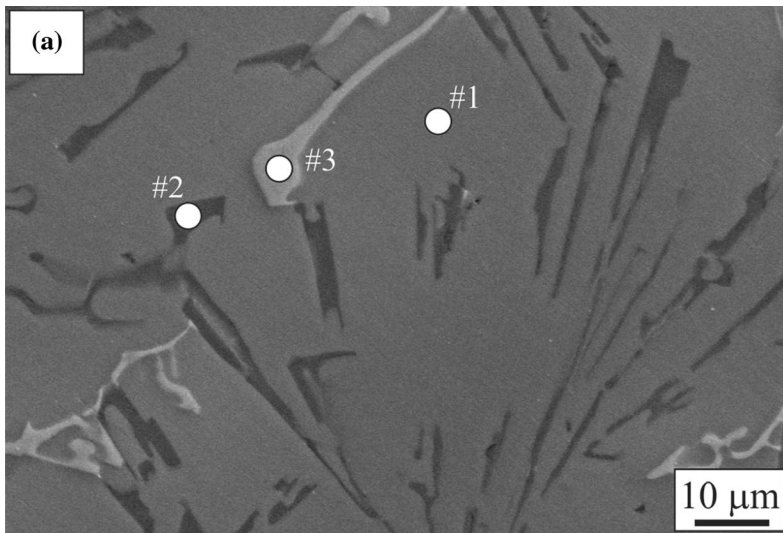


**Fig. 9** Evolution of primary dendritic spacing as a function of (a)  $\dot{T}$  and (b)  $v$ ; evolution of secondary dendritic spacing as a function of (c)  $\dot{T}$  and (d)  $v$ ; and evolution of tertiary dendritic spacing as a function of (e)  $\dot{T}$  and (f)  $v$ .  $R^2$  is the coefficient of determination.

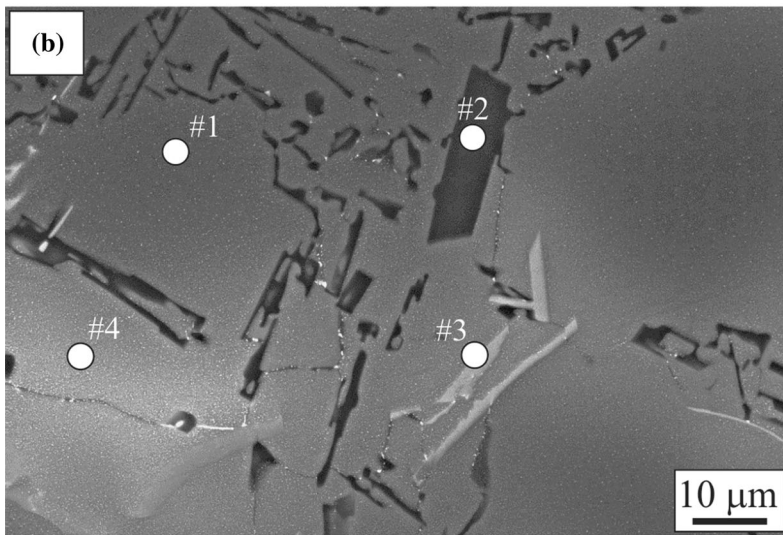
dendrites (Fig. 7). As the alloy Zn content increased, some modifications in dendritic growth occurred. Tertiary dendritic arms did not develop in the Al-7%Si-20%Zn alloy ingot,

whereas in the other alloys ingots, stable growth of tertiary branches started for  $v < 0.87$  mm/s. For the Al-7%Si-10%Zn alloy, the secondary branches grew orthogonally in relation to

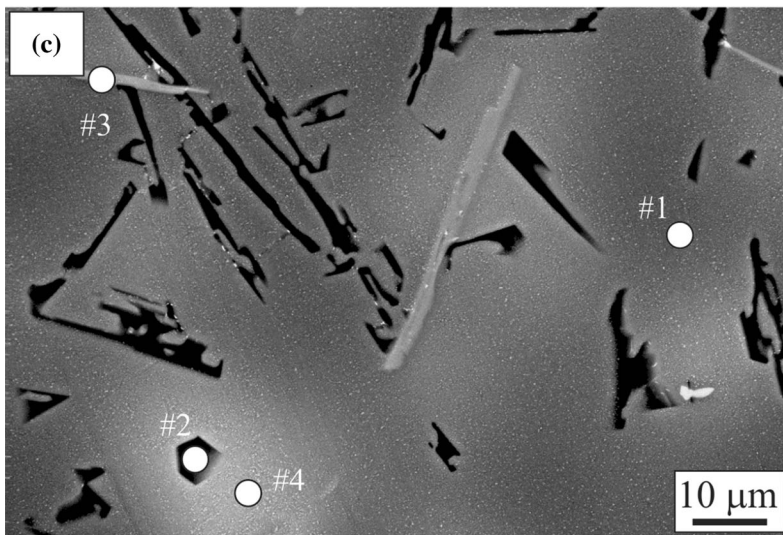




	wt. %			
	Al	Si	Zn	Fe
#1	88.46	0.83	12.71	-
#2	19.90	75.71	4.39	-
#3	57.04	8.65	7.89	26.42
	at. %			
	Al	Si	Zn	Fe
#1	93.47	0.86	5.67	-
#2	21.07	77.01	1.92	-
#3	70.10	10.21	4.00	15.69



	wt. %			
	Al	Si	Zn	Fe
#1	86.11	1.07	12.81	-
#2	1.86	98.14	-	-
#3	58.24	15.09	6.34	20.32
#4	71.55	0.40	28.05	-
	at. %			
	Al	Si	Zn	Fe
#1	93.16	1.12	5.72	-
#2	1.94	98.06	-	-
#3	68.38	17.02	3.07	11.53
#4	85.67	0.46	13.87	-



	wt. %			
	Al	Si	Zn	Fe
#1	79.48	0.76	19.76	-
#2	28.49	59.69	11.82	-
#3	62.71	12.56	8.10	16.63
#4	66.78	0.54	32.68	-
	at. %			
	Al	Si	Zn	Fe
#1	89.94	0.83	9.23	-
#2	31.41	63.21	5.38	-
#3	72.78	14.01	3.88	9.33
#4	82.66	0.64	16.70	-

Fig. 10 SEM-EDS results of: (a) Al-7%Si-10%Zn, (b) Al-7%Si-15%Zn and (c) Al-7%Si-20%Zn alloys

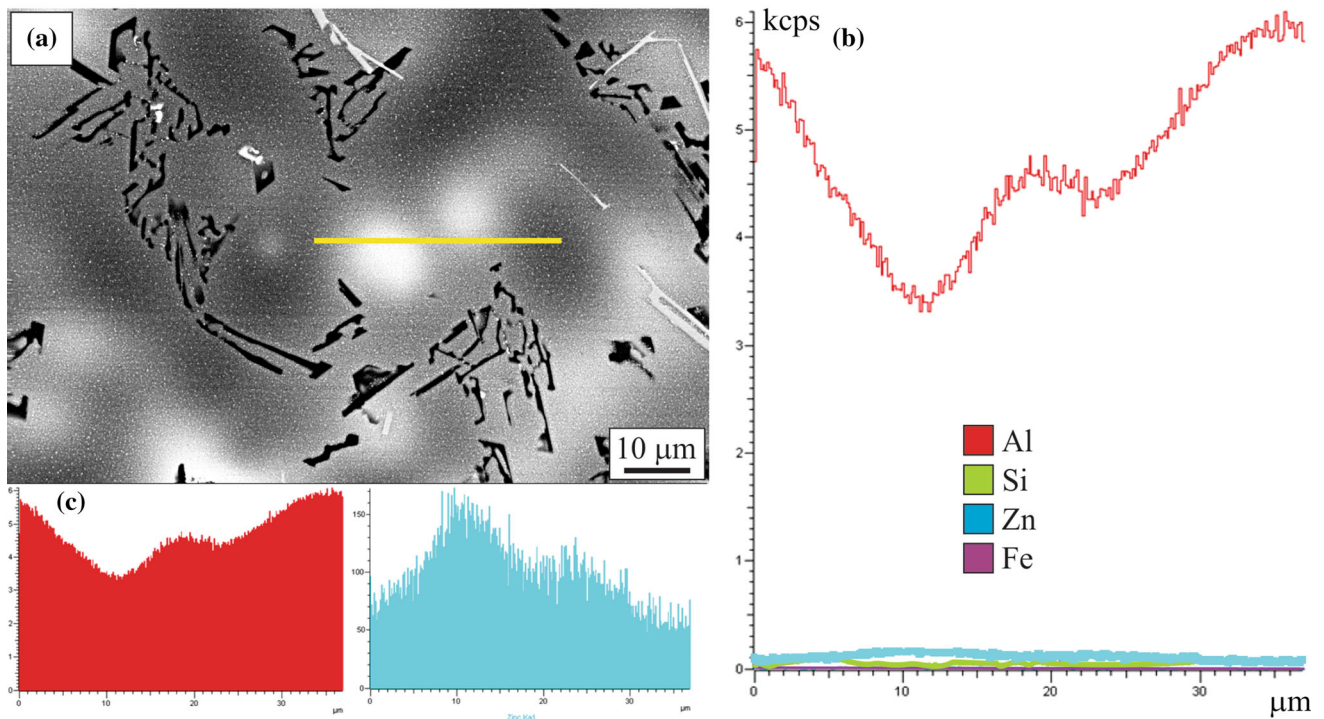


**Fig. 11** SEM-EDS results, employing line scan, of the Al-7%Si-15%Zn alloy. (a) The yellow line is the line scan, (b) distribution of all elements and (c) intensity of Al and Zn

the primary branches. On the other hand, in the Al-7%Si-15% Zn alloy ingot, the samples that solidified at  $\dot{T} > 1.5$  °C/s and  $v > 0.63$  mm/s exhibited the secondary branches tilted in a direction opposite to that of heat extraction; and in the Al-7% Si-20%Zn alloy ingot, tilted secondary branches were found in the entire microstructure. The change in secondary branch growth is more remarkable in the longitudinal view of the samples, as can be seen in Fig. 8.

Oliveira and collaborators (Ref 40) established a possible relationship between the crystal structure of the alloying element and the dendritic morphology of binary Al alloys. The dendrite with orthogonal branches is formed when the alloying element has a face-centered cubic structure or similar, whereas Si has a diamond cubic structure. For alloying elements having a hexagonal close-packed structure, like Zn, tilted secondary branches and absence of tertiary branches seem to be induced. In the last relation, elements with body-centered cubic structure seem to induce the formation of cells instead of dendrites. In addition, Friedli and collaborators (Ref 41) explained that there is a morphology dependence with the anisotropy of solid/liquid interface, for which solutes having an anisotropy higher than that of the solvent can easily disturb primary phase growth. Al has low anisotropy, around 1% (Ref 42), while that of Zn is close to 30% (Ref 43), showing a high capability to influence the growth of the primary  $\alpha$ -Al phase. However, Acer and collaborators (Ref 20, 44) studied a series of Al-Zn alloys, using Bridgman growth, and reported more than one type of morphology for the primary phase. For Al- $x$ % Zn alloys, where  $x$  was 1, 3, 5, 7, or 10, grown at a constant thermal gradient of 10.3 °C/mm, the primary phase grew with a cellular morphology for  $v < 0.01$  mm/s, followed by a cell-to-dendrite transition above this growth rate, and evolving to dendrites for  $v > 40$  mm/s. In these Al-Zn alloys, most of the

dendrites were reported to have orthogonal secondary branches. In contrast, only dendrites were detected for the Al-20%Zn alloy, even for lowest  $v$ , and the majority of the secondary branches were tilted. Other studies about directional solidification of Al-Zn alloys (Ref 43, 45, 46) confirmed the orthogonal secondary branches in the Al-10%Zn alloy and tilted branches in the Al-25%Zn alloy. In this sense, the influence of Zn over the microstructure is not restricted to its physical and chemical properties, but it also depends on the solidification thermal parameters and on the alloy Zn content.

The gradual modification of the dendrites, following the increase in the alloy Zn content, can be related to the Zn/Si proportion in Al-7%Si- $x$ %Zn alloys. When the proportion was 1.4, the dendrites were like those found in Al-Si alloys; increasing to 2.1, at  $\dot{T} > 1.5$  °C/s or  $v > 0.63$  mm/s, the secondary branches tilted; and entirely tilted secondary branches, without tertiary branches, were achieved with Zn/Si = 2.9. It seems that the inception of the dendritic modification is in the range  $1.4 < \text{Zn/Si} < 2.1$ .

The evolution of the dendritic arm spacings as a function of  $\dot{T}$  and  $v$  (Fig. 9), followed power-law functions, whose exponents are the same reported in the literature (Ref 33, 47). In general,  $\lambda_1$ ,  $\lambda_2$ , and  $\lambda_3$  became more refined as  $\dot{T}$  and  $v$  increased, and the Al-7%Si-15%Zn alloy showed lower dendritic spacings in relation to the other examined alloys. For the Al-7%Si-10%Zn alloy, the correlations between dendritic spacings and  $\dot{T}$  (Fig. 9a,c,e) were always in the upper profile ( $\lambda_1=546 \dot{T}^{-0.55}$ ,  $\lambda_2=27 \dot{T}^{-1/3}$ ,  $\lambda_3=29 \dot{T}^{-0.25}$ ) i.e., coarser dendritic spacings, and the correlations with  $v$  (Fig. 9b, d, f) are the same of that of the Al-7%Si-15%Zn alloy. The dendritic spacings of the Al-7%Si-20%Zn alloy exhibited two behaviors; while  $\lambda_1$  was in the lower profile (more refined,  $\lambda_1=271 \dot{T}^{-0.55}$ ),  $\lambda_2$  was in the upper profile (coarser,  $\lambda_2=27 \dot{T}^{-1/3}$ ). When



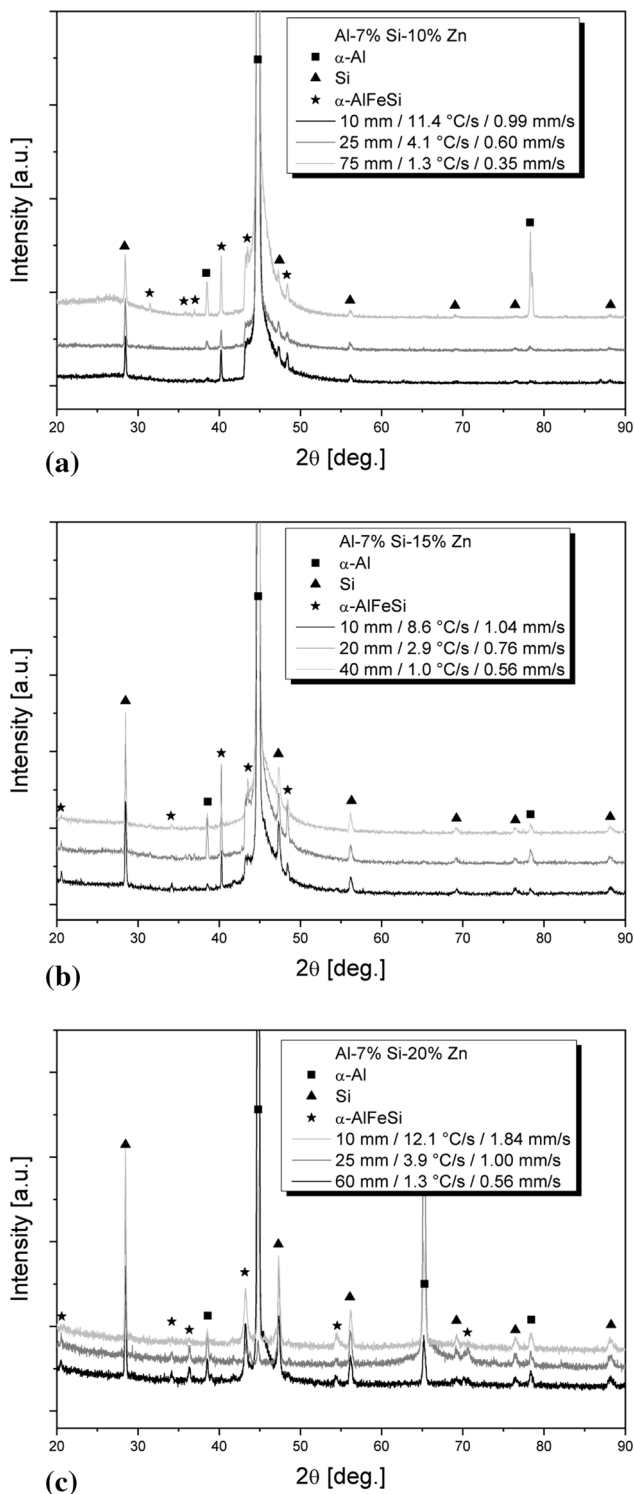


**Fig. 12** XRD results of: (a) Al-7%Si-10%Zn, (b) Al-7%Si-15%Zn and (c) Al-7%Si-20%Zn alloys

compared with the results from a previous study with a binary Al-7%Si alloy (Ref 39, 48), the addition of Zn led to coarsening of  $\lambda_1$  and  $\lambda_3$ , but to refinement of  $\lambda_2$ . Another effect was the change in the exponents of the  $\lambda_3$  correlations, which for the Al-7%Si-x%Zn alloys are associated with lower coarsening with the decrease in  $\dot{T}$  and  $v$ . For binary alloys, it is usual that  $\lambda_1$  and  $\lambda_3$  correlations share the same classical exponents (0.55 and

1.10 for  $\dot{T}$  and  $v$ , respectively). However, a third element may affect the coarsening of the dendrites, mainly the tertiary branches, which are the closest to the interdendritic liquid, rich in solute. Lower exponents for  $\lambda_3$  have been reported in Al-Si-Cu (Ref 49, 50) and Al-Si-Ni (Ref 47) alloys.

As can be seen in Fig. 9(e)-(f), well-developed tertiary branches were found in the Al-7%Si-(10, 15)%Zn alloys for  $v \leq 0.80$  mm/s but not for a specific range of  $\dot{T}$ . The absence of third-order ramifications in samples close to the cooled base of the ingots is curious. On the other hand, working with phase-field modeling of directional solidification, Zhang and collaborators (Ref 51) verified that the tertiary branches only appeared when  $\lambda_1$  was higher than 72  $\mu\text{m}$ . Sá and collaborators (Ref 52) adopted a parametric factor, involving cooling rate and solute content, to determine the onset of tertiary branches growth in binary Al alloys. For Al-7%Si-x%Zn alloys, as the correlation between  $\lambda_1$  and  $v$  is given by a single growth law, the minimum  $\lambda_1$  criterion can be confirmed with the critical value being 130  $\mu\text{m}$ , while the parametric factor seems not to apply to ternary alloys. In parallel to the development of tertiary branches, after the critical value of  $v$ , the measured  $\lambda_2$  was always above the experimental correlation in relation to  $v$  (Fig. 9d). In this case, besides the usual coarsening mechanisms, such as dissolution of small branches and coalescence, the increase in  $\lambda_2$  seems to be accelerated by the growth of tertiary branches. Tertiary branch growth was favored due to the parallel alignment to the heat flow direction. Thus,  $\lambda_2$  and  $\lambda_3$  are of the same order of magnitude, despite the fact that the tertiary branches emerged after the secondary ones.

In Fig. 10, the SEM-EDS results of some samples are depicted. Again, three phases were identified:  $\alpha$ -Al matrix (gray phase), with solid solution of Si and Zn, Si (dark phase), and plate-like AlFeSi intermetallic (light gray phase). The solubility of Si and Zn in  $\alpha$ -Al, at room temperature, is less than 0.1% (Ref 18, 22, 53), however, the presence of these elements in the matrix was over 0.5%. In the Al-7%Si-x%Zn alloys, the maximum supersaturated solid solution of Si in  $\alpha$ -Al was 1.1% for  $\dot{T} > 8.6$  °C/s, decreasing to 0.7% for  $\dot{T} < 1.3$  °C/s. In the case of Zn, the supersaturation seems not to be sensitive to the thermal parameters but related to the alloy Zn content. On average, the amount of Zn in the matrix was 11.5, 13.0, and 17.2% in the alloys with 10, 15, and 20% Zn, respectively. According to the partial phase diagram (Fig. 1a), Zn remains as solid solution until 150-220 °C, transforming to  $\eta$ -Zn below this range. It is known that the phase transformations in solid-state demands conditions close to equilibrium. It seems that the cooling rates imposed by the water-cooled mold were able to hinder the diffusion of Zn in the Al-rich solid matrix along the length of the ingot, thus, restraining the formation of  $\eta$ -Zn. Another fact that helps the supersaturation of Zn is that its atomic radius is smaller than that of Al (1.332 Å against 1.432 Å (Ref 54)).

Although the SEM-EDS results pointed a little content of Zn in the AlFeSi phase, a quaternary intermetallic has not been described in the literature (Ref 55-57). Actually, Liu and collaborators (Ref 55) studied the Al-Si-Zn-Fe system and reported a maximum solubility of 8.8% Zn in the AlFeSi-type intermetallic, and Pan and collaborators (Ref 57) reported, for the Zn-Al-Si-Fe system, an AlFeSi phase with 14.7% Zn. In the Al-7%Si-x%Zn alloys ingots, it was found that the highest value of Zn in the AlFeSi phase was 9.0%. Based on the SEM results (Fig. 10), despite the partition coefficients of Zn and Fe, respectively, 0.44 (Ref 58) and 0.029 (Ref 59), due to the high



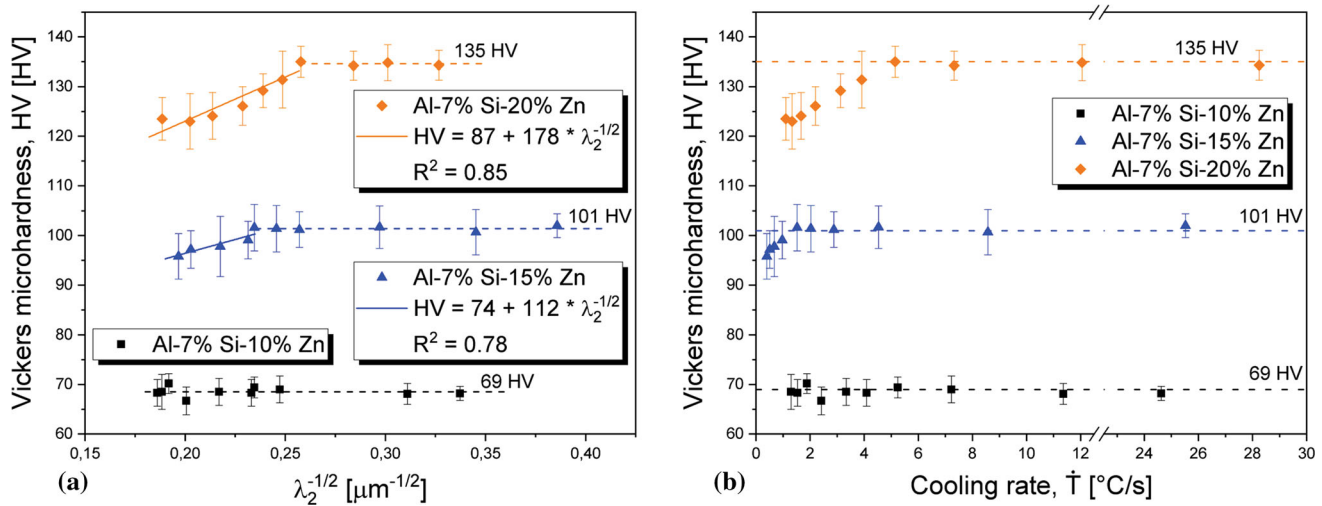


**Fig. 13** Profiles of Vickers microhardness for Al-7%Si-10%Zn, Al-7%Si-15%Zn and Al-7%Si-20%Zn alloys: (a) as a function of  $\lambda_2^{-1/2}$ , (b) as a function of  $\dot{T}$ .  $R^2$  is the coefficient of determination.

$\dot{T}$  and  $v$  all Zn was kept in solid solution and Fe was trapped in the interdendritic liquid. In other words, the solidification kinetics hampered the rejection of both Zn and Fe toward the liquid/solid interface ahead of the dendrite's tips.

In the Al-7%Si-(15, 20)%Zn alloys, white spots appeared close to the interdendritic region, as can be seen in Fig. 10(b), (c). These spots were present in all the analyzed samples of the Al-7%Si-15%Zn and Al-7%Si-20%Zn alloys ingots, and at the center of these regions, respectively, the Zn content was around 26 and 31%. In the line scan analysis (Fig. 11a, b), Si and Fe remained constant, and Zn showed a gradual variation, featuring a microsegregation profile (Fig. 11c). Once the supersaturation in the  $\alpha$ -Al phase was uniform and since the interdendritic liquid is the last portion to be solidified, after the precipitation of Si and AlFeSi phases, the solute rejection enriched the remaining liquid with Zn. Although this liquid surpassed the supersaturation limit, there were no chemical and thermodynamic conditions favoring the growth of the  $\eta$ -Zn phase. So, with the increase in solid fraction and the continuous solute rejection, a gradient of Zn was established. In Al-Zn alloys, the  $\eta$ -Zn phase is mainly formed from a eutectoid reaction, then, at low cooling rates, the white spots would transform in the Zn-rich phase. The XRD analysis (Fig. 12) confirmed that the microstructure in the Al-7%Si-x%Zn alloys was composed of  $\alpha$ -Al, Si, and  $\alpha$ -Al<sub>12</sub>Fe<sub>3</sub>Si<sub>2</sub> phases, without a trace of a Zn-rich phase. As examined, the Zn remained in solid solution in the  $\alpha$ -Al matrix and, a little fraction, in the  $\alpha$ -Al<sub>12</sub>Fe<sub>3</sub>Si<sub>2</sub> intermetallic.

The correlation between mechanical properties and microstructural parameters can be expressed in terms of a Hall-Petch type equation, replacing the grain size with the dendritic arm spacing and maintaining the reliability. According to Campbell (Ref 60), the dendritic spacing of highest order has a major influence over the mechanical properties. However,  $\lambda_3$  was not present in the Al-7%Si-20%Zn alloy ingot, and thus, it may not be used as a reference microstructural parameter for comparison purposes. Therefore,  $\lambda_2$  has been adopted as the characteristic microstructural parameter, and the evolution of

the Vickers microhardness with  $\lambda_2$  can be seen in Fig. 13(a). The hardness was the result of the contribution the Zn-supersaturated  $\alpha$ -Al dendritic matrix, the eutectic  $\alpha$ -Al+Si, and the intermetallic  $\alpha$ -AlFeSi dispersed in the eutectic mixture. The hardness of  $\alpha$ -AlFeSi is 1025 HV, as reported in the literature (Ref 61), and its high hardness also contributes to the hardness response of the alloy. The hardness of the Al-7%Si-10%Zn alloy was not influenced by refinement of the microstructure and kept equal to 69 HV. For the other alloys, the hardness is constant for refined  $\lambda_2$ , and showing a variable behavior for  $\lambda_2^{-1/2} < 0.25 \mu\text{m}^{-1/2}$ , i.e., coarser dendritic spacings. In hypoeutectic Al-Si alloys, the hardness has been reported to be weakly sensitive to the size of the dendritic spacings and more dependent on the alloy Si content (Ref 62). Previous studies with the Al-7%Si alloy reported hardness in the range of 42-49 HV (Ref 25, 63, 64) and, with the supersaturation provided by Zn, the Al-7%Si-10%Zn alloy showed a hardness of about 41% higher. So, for the Al-7%Si-x%Zn alloys, the main mechanism of reinforcement was shown to be the supersaturated solid solution and each increment of about 5% Zn to the Al-7%Si-x%Zn alloys, as shown in Fig. 13 (a), resulted in increase of about 30 HV. In this sense, in the Al-7%Si-(15, 20)%Zn alloys, the supersaturation induces a fragile behavior for the  $\alpha$ -Al phase, and the coarsening of the dendrites was accompanied by a reduction in plastic behavior. Consequently, the matrix was unable to maintain the same mechanical response, and thus, hardness decreased with the increase in  $\lambda_2$ . In terms of cooling rate (Fig. 13b), for Al-7%Si-15%Zn and Al-7%Si-20%Zn alloys ingots, the critical values of  $\dot{T}$  to achieve the highest hardness were 1.5 and 5.1  $^{\circ}\text{C/s}$ , respectively. According to the  $\lambda_2 \times \dot{T}$  correlations (Fig. 9c), the critical cooling rates results in  $\lambda_2$  around 15.7-16.6  $\mu\text{m}$ . As the Al-7% Si-20%Zn alloy ingot presented an upper  $\lambda_2$  profile, a higher  $\dot{T}$  is required to reach this refined  $\lambda_2$ . In the case of the Al-7%Si-10%Zn alloy ingot, in the studied range of  $\dot{T}$ , the hardness was not sensitive to the cooling rate.

## 4. Conclusions

- The microstructure of the Al-7%Si-x%Zn alloys was shown to be characterized by a dendritic  $\alpha$ -Al matrix, with the interdendritic region composed of  $\alpha$ -Al, Si, and an AlFeSi-type intermetallic. The decrease in solidification cooling rate ( $\dot{T}$ ) and growth rate ( $v$ ) resulted in the coarsening of the dendrites. With the increase in the alloy Zn content, modifications in dendritic growth occurred. Tertiary dendritic arms did not develop in the Al-7%Si-20%Zn alloy, whereas in the other two alloys ingots having 10 and 15%Zn, stable growth of tertiary branches started for  $v < 0.87$  mm/s. For the Al-7%Si-10%Zn alloy, the secondary branches grew orthogonally in relation to the primary branches. On the other hand, in the Al-7%Si-15%Zn alloy ingot, the samples solidified at  $\dot{T} > 1.5$  °C/s and  $v > 0.63$  mm/s exhibited the secondary branches tilted in a direction opposite to that of heat extraction and in the Al-7%Si-20%Zn alloy, tilted secondary branches were found in the entire microstructure.
- Dendritic scaling laws were experimentally determined relating  $\lambda_1; \lambda_2$  and  $\lambda_3$  [ $\mu\text{m}$ ] to  $\dot{T}$  [°C/s] and  $v$  [mm/s], that is:

$$\text{Al-7\%Si-10\%Zn: } \lambda_1=546 \dot{T}^{-0.55}; \lambda_2=27 \dot{T}^{-1/3}; \lambda_3=29 \dot{T}^{-0.25}$$

$$\text{Al-7\%Si-15\%Zn: } \lambda_1=271 \dot{T}^{-0.55}; \lambda_2=19 \dot{T}^{-1/3}; \lambda_3=21 \dot{T}^{-0.25}$$

$$\text{Al-7\%Si-20\%Zn: } \lambda_1=271 \dot{T}^{-0.55}; \lambda_2=27 \dot{T}^{-1/3}$$

$$\text{Al-7\%Si-10\%Zn: } \lambda_1=121 v^{-1.1}; \lambda_2=12 v^{-2/3}; \lambda_3=16 v^{-0.50}$$

$$\text{Al-7\%Si-15\%Zn: } \lambda_1=121 v^{-1.1}; \lambda_2=12 v^{-2/3}; \lambda_3=16 v^{-0.50}$$

$$\text{Al-7\%Si-20\%Zn: } \lambda_1=121 v^{-1.1}; \lambda_2=16 v^{-2/3}$$

- For the Al-7%Si-x%Zn alloys, the main mechanism of reinforcement was shown to be the supersaturated solid solution. The hardness of the Al-7%Si-10%Zn alloy was not influenced by refinement of the dendritic spacings and kept equal to 69 HV. Each further increment of about 5% Zn to the Al-7%Si-10%Zn alloys, resulted in increase of about 30 HV. In this sense, in the Al-7%Si-(15, 20) %Zn alloys, the supersaturation induced a fragile behavior for the  $\alpha$ -Al phase, and the coarsening of the dendrites was accompanied by a reduction in the plastic behavior. Consequently, the matrix was unable to maintain the same mechanical response, and thus, hardness decreased with the increase in dendritic spacings.

## Acknowledgments

The authors are grateful to LNNano (Brazilian Nanotechnology National Laboratory) for the use of its facilities (XRD facility).

## Funding

This study was financed by: National Council for Scientific and Technological Development – CNPq

## Data Availability

Data will be made available on request.

## Declarations

## Conflict of interest

The authors declare no potential conflicts of interest with respect to the research and/or publication of this article.

## References

1. F.C. Robles-Hernandez, J.M.H. Ramirez and R. Mackay, *Al-Si Alloys: Automotive, Aeronautical, and Aerospace Applications*, 1st ed. Springer, Cham, 2017
2. J.-G. Jung, S.-H. Lee, J.-M. Lee, Y.-H. Cho, S.-H. Kim and W.-H. Yoon, Improved Mechanical Properties of Near-Eutectic Al-Si Piston Alloy Through Ultrasonic Melt Treatment, *Mater. Sci. Eng. A*, 2016, **669**, p 187–195.
3. V. Casalegno, M. Salvo, S. Rizzo, L. Goglio, O. Damiano and M. Ferraris, Joining of Carbon Fibre Reinforced Polymer to Al-Si Alloy for Space Application, *Int. J. Adhes. Adhes.*, 2018, **82**, p 146–152.
4. W. Kasprzak, F. Czerwinski, M. Niewczas and D.L. Chen, Correlating Hardness Retention and Phase Transformations of Al and Mg Cast Alloys for Aerospace Applications, *J. Mater. Eng. Perform.*, 2015, **24** (3), p 1365–1378.
5. Y. Zhao, H.B. Liu and C.Y. Zhao, Experimental Study on the Cycling Stability and Corrosive Property of Al-Si Alloys as Phase Change Materials in High-Temperature Heat Storage, *Sol. Energy Mat. Sol. Cells*, 2019, **203**, p 110165.
6. N. Gokon, S. Nakamura, T. Yamaguchi and T. Kodama, Cyclic Properties of Thermal Storage/Discharge for Al-Si Alloy in Vacuum for Solar Thermochemical Fuel Production, *Energy Proc.*, 2015, **69**, p 1759–1769.
7. W. Liang, W. Tao, B. Zhu and Y. Zhang, Influence of Heating Parameters on Properties of the Al-Si Coating Applied to Hot Stamping, *Sci. China Technol. Sci.*, 2017, **60**(7), p 1088–1102.
8. C.-J. Wang and S.-M. Chen, The high-Temperature Oxidation Behavior of Hot-Dipping Al-Si Coating on Low Carbon Steel, *Surf. Coat. Tech.*, 2006, **200**(22–23), p 6601–6605.
9. J.-H. Yoo, K.-S. Yun, R.S. Kalubarme, C.-N. Park and C.-J. Park, Hydrogen Generation Using the Corrosion of Al-Sn and Al-Si Alloys in an Alkaline Solution, *Met. Mater. Int.*, 2014, **20**(4), p 619–627.
10. L. Soler, J. Macanás, M. Muñoz and J. Casado, Aluminum and Aluminum Alloys as Sources of Hydrogen for Fuel Cell Applications, *J. Power Sour.*, 2007, **169**(1), p 144–149.
11. V. Srinivas, A.K. Singh, V.G. Krishna and G.M. Reddy, Vacuum Brazing of Dissimilar Component of AA2219 and AISI 304 by a Low Melting Al-18Ag-20Cu-5Si-0.2Zn Braze Alloy, *J. Mater. Process. Technol.*, 2018, **252**, p 1–12.
12. Z. Niu, J. Huang, K. Liu, F. Xu, S. Chen and X. Zhao, Brazing of 6061 Aluminum Alloy with the Novel Al-Si-Ge-Zn Filler Metal, *Mater. Lett.*, 2016, **179**, p 47–51.
13. K. Suzuki, M. Kagayama and Y. Takeuchi, Eutectic Phase Equilibrium of Al-Si-Zn System and its Applicability for Lower Temperature Brazing, *J. Jpn. Inst. Light Met.*, 1983, **43**(10), p 533–538. (in Japanese)
14. J. Yang, S. Xue, H. Liu, P. Xue and W. Dai, Effects of Silicon on Microstructures and Properties of Al-40Zn-xSi Filler Metal, *Rare Metal Mater. Eng.*, 2016, **45**(2), p 333–338.
15. W. Luo, L.T. Wang, Q.M. Wang, H.L. Gong and M. Yan, A New Filler Metal with Low Contents of Cu for High Strength Aluminum Brazed Joints, *Mater. Des.*, 2014, **63**, p 263–269.
16. Z. Niu, J. Huang, H. Yang, S. Chen and X. Zhao, Preparation and Properties of a Novel Al-Si-Ge-Zn Filler Metal for Brazing Aluminum, *J. Mater. Eng. Perform.*, 2015, **24**(6), p 2327–2334.
17. L.C. Tsao, M.J. Chiang, W.H. Lin, M.D. Cheng and T.H. Chuang, Effects of Zinc Additions on the Microstructure and Melting Temperatures of Al-Si-Cu Filler Metals, *Mater. Charact.*, 2002, **48**(4), p 341–346.

18. J.L. Murray, The Al-Zn (aluminum-zinc) System, *Bull. Alloy Phase Diagr.*, 1983, **4**(1), p 55–73.
19. O. Gusakova, V. Shepelevich, D. Alexandrov and I. Starodumov, Rapid Quenching Effect on the Microstructure of Al-Si Eutectic Zn-Doped Alloy, *J. Cryst. Growth*, 2020, **531**, p 125333.
20. E. Acer, E. Çadırli, H. Erol, H. Kaya and M. Gündüz, Effects of Growth Rates and Compositions on Dendrite Arm Spacings in Directionally Solidified Al-Zn Alloys, *Metall. Mater. Trans. A*, 2017, **48**(12), p 5911–5923.
21. S. García-Villarreal, A. Chávez-Valdez, K.J. Moreno, C. Leyva, J.A. Aguilar-Martínez, A. Hurtado and A. Arizmendi-Morquecho, Microstructural and Mechanical Characterization of Al-Zn-Si Nanocomposites, *Mater. Charact.*, 2013, **83**, p 187–197.
22. A.A. Mazilkin, B.B. Straumal, E. Rabkin, B. Baretzky, S. Enders, S.G. Protasova, O.A. Kogtenkova and R.Z. Valiev, Softening of Nanostructured Al-Zn and Al-Mg Alloys After Severe Plastic Deformation, *Acta Mater.*, 2006, **54**(15), p 3933–3939.
23. F. Mao, S. Wei, C. Chen, C. Zhang, X. Wang and Z. Cao, Modification of the Silicon Phase and Mechanical Properties in Al-40Zn-6Si Alloy with Eu Addition, *Mater. Des.*, 2020, **186**, p 108268.
24. T. Hoshina, S. Amano, M. Koushima and K. Ishikura, Development of High Strength Aluminum-Zinc-Silicon Alloy Bearing with Polymer Overlay, *SAE Tech. Pap.*, 2019 <https://doi.org/10.4271/2019-01-0179>
25. Y. Alemdağ and M. Beder, Microstructural, Mechanical and Tribological Properties of Al-7Si-(0–5) Zn Alloys, *Mater. Des.*, 2014, **63**, p 159–167.
26. T. Nirasawa, M. Yasui, O. Ishigo, Y. Kagohara and M. Fujita, A Study of Lead-free Al-Zn-Si Alloy Bearing with Overlay for Recent Automotive Engines, *SAE Tech. Pap.*, 2009 <https://doi.org/10.4271/2009-01-1054>
27. J.R. Davis, *Alloying: Understanding the basis*, 1st ed., ASM International, Materials Park, (2001)
28. B. Wang, S. Xue, J. Wang and Z. Lin, Effect of Combinative Addition of Mischmetal and Titanium on the Microstructure and Mechanical Properties of Hypoeutectic Al-Si Alloys Used for Brazing and/or Welding Consumables, *J. Rare Earth*, 2017, **35**(2), p 193–202.
29. W. Dai, S. Xue, F. Ji, J. Lou, B. Sun and S. Wang, Brazing 6061 Aluminum Alloy with Al-Si-Zn Filler Metals Containing Sr, *Int. J. Min. Met. Mater.*, 2013, **20**(4), p 365–370.
30. I.V. Shutov, L.V. Kamaeva, M.D. Krivilyov, C.-N. Yu, S.Dj. Mesarovic and D.P. Sekulic, Effect of Processing Parameters on Microstructure in Brazing of Al-Si Alloys, *J. Cryst. Growth*, 2020, **530**, p 125287.
31. M. Dias, R. Oliveira, R. Kakitani, N. Cheung, H. Henein, J.E. Spinelli and A. Garcia, Effects of Solidification Thermal Parameters and Bi Doping on Silicon Size, Morphology and Mechanical Properties of Al-15wt.% Si-3.2wt.% Bi and Al-18wt.% Si-3.2wt.% Bi Alloys, *J. Mater. Res. Technol.*, 2020, **9**(3), p 3460–3470.
32. R.V. Reyes, T.S. Bello, R. Kakitani, T.A. Costa, A. Garcia, N. Cheung and J.E. Spinelli, Tensile Properties and Related Microstructural Aspects of Hypereutectic Al-Si Alloys Directionally Solidified Under Different Melt Superheats and Transient Heat Flow Conditions, *Mater. Sci. Eng. A*, 2017, **685**, p 235–243.
33. C. Brito, T.A. Costa, T.A. Vida, F. Bertelli, N. Cheung, J.E. Spinelli and A. Garcia, Characterization of Dendritic Microstructure, Intermetallic Phases, and Hardness of Directionally Solidified Al-Mg and Al-Mg-Si Alloys, *Metall. Mater. Trans. A*, 2015, **46**(8), p 3342–3355.
34. M. Gündüz and E. Çadırli, Directional Solidification of Aluminium-Copper Alloys, *Mater. Sci. Eng. A*, 2002, **327**(2), p 167–185.
35. Y.H. Cho, H.W. Kim, W. Kim, D.A. Jo and J.M. Lee, The Effect of Ni Additions on the Microstructure and Castability of Low Si Added Al Casting Alloys, *Mater. Today-Proc.*, 2015, **2**(10), p 4924–4930.
36. H. Becker, T. Bergh, P.E. Vullum, A. Leineweber and Y. Li, Effect of Mn and Cooling Rates on  $\alpha$ -,  $\beta$ -,  $\delta$ -Al-Fe-Si Intermetallic Phase Formation in a Secondary Al-Si alloy, *Materialia*, 2019, **5**, p 100198.
37. S.G. Irizalp and N. Saklakoglu, Effect of Fe-Rich Intermetallics on the Microstructure and Mechanical Properties of Thixoformed A380 Aluminum Alloy, *Eng. Sci. Technol. Int. J.*, 2014, **17**(2), p 58–62.
38. A.E. Ares and C.E. Schvezov, Influence of Solidification Thermal Parameters on the Columnar-to-Equiaxed Transition of Aluminum-Zinc and Zinc-Aluminum Alloys, *Metall. Mater. Trans. A*, 2007, **38**(7), p 1485–1499.
39. M.D. Peres, C.A. Siqueira and A. Garcia, Macrostructural and Microstructural Development in Al-Si Alloys Directionally Solidified Under Unsteady-State Conditions, *J. Alloys Compd.*, 2004, **381**(1–2), p 168–181.
40. R. Oliveira, R. Kakitani, L.R. Ramos, D.L. Gonçalves, A. Garcia and N. Cheung, The Roles of Mn and Ni Additions to Fe-Contaminated Al in Neutralizing Fe and Stabilizing the Cellular  $\alpha$ -Al Microstructure, *J. Sustain. Met.*, 2019, **5**(4), p 561–580.
41. J. Friedli, P. Di Napoli, M. Rappaz and J.A. Dantzig, Phase-Field Modeling of the Dendrite Orientation Transition in Al-Zn alloys, *IOP Conf Ser. Mater. Sci.*, 2012, **33**, p 012111.
42. S. Liu, R.E. Napolitano and R. Trivedi, Measurement of Anisotropy of Crystal-Melt Interfacial Energy for a Binary Al-Cu Alloy, *Acta Mater.*, 2001, **49**(20), p 4271–4276.
43. J. Friedli, J.L. Fife, P. Di Napoli and M. Rappaz, Dendritic Growth Morphologies in Al-Zn Alloys – Part I: X-ray Tomographic Microscopy, *Metall. Mater. Trans. A*, 2013, **44**(12), p 5522–5531.
44. E. Acer, E. Çadırli, H. Erol, H. Kaya, M. Şahin and M. Gündüz, Effect of Growth Velocity and Zn Content on Microhardness in Directionally Solidified Al-Zn Alloys, *Mater. Res.*, 2018, **21**(6), p e20180337.
45. Z. Chen, E. Wang and X. Hao, Microstructure and Orientation Evolution in Unidirectional Solidified Al-Zn Alloys, *Mater. Sci. Eng. A*, 2016, **667**, p 1–8.
46. F. Gonzales and M. Rappaz, Dendrite Growth Directions in Aluminum-Zinc Alloys, *Metall. Mater. Trans. A*, 2006, **37**(9), p 2797–2806.
47. R. Kakitani, C.B. Cruz, T.S. Lima, C. Brito, A. Garcia and N. Cheung, Transient Directional Solidification of a Eutectic Alloy: Macrostructure, Microstructure, Dendritic Growth and Hardness, *Materialia*, 2019, **7**, p 100358.
48. D.M. Rosa, J.E. Spinelli and A. Garcia, Tertiary Dendrite Arm Spacing During Downward Transient Solidification of Al-Cu and Al-Si Alloys, *Mater. Lett.*, 2006, **60**(15), p 181–1874.
49. L.A.S. Baptista, K.G. Paradela, I.L. Ferreira, A. Garcia and A.F. Ferreira, Experimental Study of the Evolution of Tertiary Dendritic Arms and Microsegregation in Directionally Solidified Al-Si-Cu Alloys Castings, *J. Mater. Res. Technol.*, 2019, **8**(1), p 1515–1521.
50. B.M.C. Donadoni, L.F. Gomes, A. Garcia and J.E. Spinelli, Tailoring of Microstructures and Tensile Properties in the Solidification of Al-11Si-(xCu) Brazing Alloys, *Metals*, 2018, **8**(10), p 784.
51. B. Zhang, Y. Zhao, W. Chen, Q. Xu, M. Wang and H. Hou, Phase Field Simulation of Dendrite Sidebranching During Directional Solidification of Al-Si Alloy, *J. Alloys Compd.*, 2019, **522**, p 183–190.
52. F. Sá, O.L. Rocha, C.A. Siqueira and A. Garcia, The Effect of Solidification Variables on Tertiary Dendrite Arm Spacing in Unsteady-State Directional Solidification of Sn-Pb and Al-Cu Alloys, *Mater. Sci. Eng. A*, 2004, **373**(1–2), p 131–138.
53. J.L. Murray and A.J. McAlister, The Al-Si (aluminum-silicon) System, *Bull. Alloy Phase Diagr.*, 1984, **5**(1), p 74–83.
54. S. Sivasankaran, K.R. Ramkumar, H.R. Ammar, F.A. Al-Mufadi, A.S. Alaboodi and O.M. Irfan, Microstructural Evolutions and Enhanced Mechanical Performance of Novel Al-Zn Die-Casting Alloys Processed by Squeezing and Hot Extrusion, *J. Mater. Process. Tech.*, 2021, **292**, p 117063.
55. L. Liu, X. Pan, L. Lu, Y. Liu, X. Su and J. Wang, Phase Equilibria of 600 °C Isothermal Section of Zn-Al-Fe-Si Quaternary System, *J. Phase Equilibria Diffus.*, 2016, **37**(6), p 693–701.
56. V. Raghavan, Al-Fe-Si-Zn (Aluminum-Iron-Silicon-Zinc), *J. Phase Equilibria Diffus.*, 2011, **32**(2), p 158–159.
57. S. Pan, F. Yin, M. Zhao, Y. Liu and X. Su, The Zinc-Rich Corner of the 450 °C Isothermal Section of the Zn-Al-Fe-Si Quaternary System, *J. Alloys Compd.*, 2009, **470**(1–2), p 600–605.
58. J. Feng, W.D. Huang, X. Lin, Q.Y. Pan, T. Li and Y.H. Zhou, Primary Cellular/Dendritic Spacing Selection of Al-Zn Alloy During Unidirectional Solidification, *J. Cryst. Growth*, 1999, **197**(1–2), p 393–395.
59. P.R. Goulart, K.S. Cruz, J.E. Spinelli, I.L. Ferreira, N. Cheung and A. Garcia, Cellular Growth During Transient Directional Solidification of Hypoeutectic Al-Fe Alloys, *J. Alloys Compd.*, 2009, **470**(1–2), p 589–599.
60. J. Campbell, *Complete Casting Handbook*, 2nd ed. Butterworth-Heinemann, Oxford, 2015
61. J.L. Song, S.B. Lin, C.L. Yang, C.L. Fan and G.C. Ma, Analysis of Intermetallic Layer in Dissimilar TIG Welding-Brazing Butt Joint of Aluminum Alloy to Stainless Steel, *Sci. Technol. Weld. Joi.*, 2010, **15**(3), p 213–218.



62. S.P. Nikaronov, L.I. Derkachenko, B.K. Kardashev, B.N. Korchunov, V.N. Osipov and V.V. Shpeizman, Structural and Physicomechanical Properties of Directionally Crystallized Aluminum-Silicon Alloys, *Phys. Solid State.*, 2013, **55**(6), p 1207–1213.
63. Ş Bayraktar and F. Afyon, Machinability Properties of Al-7Si, Al-7Si-4Zn and Al-7Si-4Zn-3Cu Alloys, *J. Braz. Soc. Mech. Sci.*, 2020, **42**(4), p 187.
64. S. Kumar, M. Chakraborty, V.S. Sarma and B.S. Murty, Tensile and Wear Behaviour of in situ Al-7Si/TiB<sub>2</sub> Particulate Composites, *Wear*, 2008, **265**(1–2), p 134–142.

**Publisher's Note** Springer Nature remains neutral with regard to jurisdictional claims in published maps and institutional affiliations.